Published online November 30, 2017

Special Section: Lysimeters in Vadose Zone Research

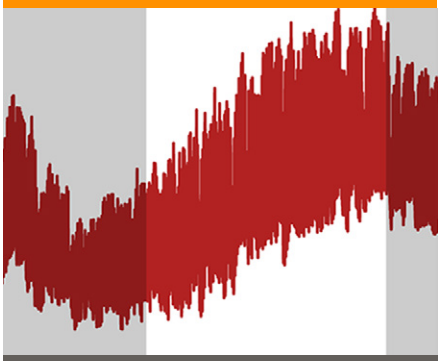

Water Distribution in an Arid Zone Soil: Numerical Analysis of Data from a Large Weighing Lysimeter

J. Dijkema, J.E. Koonce, R.M. Shillito, T.A. Ghezzehei, M. Berli,* M.J. van der Ploeg, and M.Th. van Genuchten

Although desert soils cover approximately one third of the Earth's land surface, surprisingly little is known about their physical properties and how those properties affect the ecology and hydrology of arid environments. The main goal of this study was to advance our understanding of desert soil hydrodynamics. For this purpose, we developed a process-based component within HYDRUS-1D to describe the moisture dynamics of an arid zone soil as a function of water fluxes through the soil surface. A modified van Genuchten model for the dry end of the soil water retention curve was developed to better capture the basic flow processes for very dry conditions. A scaling method was further used to account for variabilities in water retention because of changes in the bulk density vs. depth. The model was calibrated and validated using hourly soil moisture, temperature, and mass data from a 3-m-deep weighing lysimeter of the Scaling Environmental Processes in Heterogeneous Arid Soils facility at the Desert Research Institute (Las Vegas, NV). Measurements and simulations during a 1-yr period agreed better under precipitation (wetting) than under evaporation (drying) conditions. Evaporation was better simulated for wet than for dry soil surface conditions. This was probably caused by vapor-phase exchange processes with the atmosphere, which were unaccounted for and need to be further explored. Overall, the model provides a promising first step toward developing a more realistic numerical tool to quantify the moisture dynamics of arid ecosystems and their role in climate change, plant growth, erosion, and recharge patterns.

Core Ideas

- We aimed to advance our mechanistic understanding of desert soil hydrodynamics.
- We calibrated and validated a HYDRUS-1D software version on desert soil data from a weighing lysimeter.
- HYDRUS-1D is an attractive tool for virtual experiments relevant for arid ecosystems.

J. Dijkema, J.E. Koonce, R.M. Shillito, and M. Berli, Division of Hydrologic Sciences, Desert Research Institute, Las Vegas, NV 89119; J. Dijkema and M.J. van der Ploeg, Dep. of Environmental Sciences, Soil Physics and Land Management Group, Wageningen Univ., Wageningen, the Netherlands; T.A. Ghezzehei, Dep. of Life and Environmental Sciences, Univ. of California, Merced, CA 95343; M.Th. van Genuchten, Center for Environmental Studies, CEA, São Paulo State Univ., UNESP, Rio Claro, SP, Brazil, and Dep. of Earth Sciences, Utrecht Univ., Utrecht, the Netherlands. *Corresponding author (Markus.Berli@dri.edu).

Received 31 Jan. 2017.
Accepted 24 May 2017.

Citation: Dijkema, J., J.E. Koonce, R.M. Shillito, T.A. Ghezzehei, M. Berli, M.J. van der Ploeg, and M.Th. van Genuchten. 2017. Water distribution in an arid zone soil: Numerical analysis of data from a large weighing lysimeter. Vadose Zone J. doi:10.2136/vzj2017.01.0035

© Soil Science Society of America
5585 Guilford Rd., Madison, WI 53711 USA.
All rights reserved.

Abbreviations: HDU, heat dissipation unit; SEPHAS, Scaling Environmental Processes in Heterogeneous Arid Soils; TDR, time-domain reflectometry; TPHP, triple-point heat dissipation probes; WRC, water retention curve.

Desert soils cover approximately one third of the Earth's land surface (Hare, 1985), with 15 to 25% of these soils being located in arid climates that have an annual precipitation of <250 mm. Desert soils are known to affect cloud and dust formation, as well as CO_2 fluxes, which affect climate on a global scale (Austin et al., 2004; Huxman et al., 2004; Morgan et al., 2004; Bhattachan et al., 2012). Desert soils also support fragile ecosystems with flora and fauna that have adapted to limited water resources (Devitt et al., 2011; Kidron and Gutschick, 2013; Moreno-de las Heras et al., 2016). Demands on desert soils continue to increase because of an increase in the global population, and as a result of human activities such as agricultural and horticultural operations, construction, waste disposal, and recreation (Dregne et al., 1991; D'Odorico et al., 2013). Some of the fastest growing cities in the world are now in arid areas; their rapid development is often coupled with above-average water use per capita (Kenny and Juracek, 2012).

Despite the considerable extent of desert soils, relatively little is known about their moisture dynamics in space and time. This may be because deserts were previously considered unproductive for forestry and agriculture unless irrigated. Most hydrologic studies of desert soils have focused on deep infiltration (i.e., tens to hundreds of meters deep) to assess groundwater recharge or contaminant transport processes (Gee et al., 1994; Andraski,

1997; Constantz et al., 2003; Gee et al., 2005; Scanlon et al., 2005; Andraski et al., 2014) and have overlooked the near-surface soil environment (i.e., the top centimeters to meters). However, the near-surface environment controls the infiltration, runoff, storage, and evapotranspiration of sparse precipitation in arid climates (Koonce, 2016).

The overarching goal of this study was to advance our mechanistic understanding of the moisture dynamics of near-surface desert soils. We were particularly interested in moisture dynamics as a function of precipitation and evaporation within the top few meters of an arid soil. To evaluate these dynamics, we compared measured soil moisture and temperature data from a 3-m-deep weighing lysimeter located in the Mojave Desert of southern Nevada with numerical simulations using a process-based soil physical model implemented in the HYDRUS-1D software package (Simunek et al., 2016). The weighing lysimeter is part of the Scaling Environmental Processes in Heterogeneous Arid Soils (SEPHAS) facility in Boulder City, NV, constructed and managed by the Desert Research Institute (Chief et al., 2009). The lysimeter has been operational since 2008 and has collected >8 yr of data on precipitation, evaporation, soil moisture and temperature, and other relevant environmental parameters. The controlled conditions of the SEPHAS lysimeter experiment allow us to study hydrological processes of arid soils under well-defined initial and boundary conditions. The resulting database provides a unique opportunity to test the validity of conceptual and mathematical models simulating vadose zone water flow and heat transfer processes that are typical of arid and semiarid regions. We used the data to test the capability of the HYDRUS-1D software package (Šimůnek et al., 2016) to capture the strong coupling of water and heat transport processes in the lysimeter, as well as unsaturated flow near the lowest extreme of the soil moisture range.

Materials and Methods

Study Site

The study was conducted at the SEPHAS weighing lysimeter facility in Boulder City (35.96° N, 114.85° W), which is ~40 km southeast of Las Vegas, NV. The facility is located in the Mojave Desert at an elevation of 768 m. The average annual precipitation is 141 mm, whereas average daily temperatures range from 8.1°C in January to 31.7°C in July (1931–2005) (Western Regional Climate Center, 2017). The core of the SEPHAS facility consists of three weighing lysimeter tanks filled with desert soil from a study site in nearby Eldorado Valley, which is ~8 km southwest of the facility. Our study focused on only one of the three lysimeters. Soils at the Eldorado Valley study site developed from volcanic parent material (mainly andesite and rhyolite) that was deposited on a south-facing, shallow-sloped alluvial fan (0–15% slope angle) from the nearby McCullough and Highland Ranges (Chief et al., 2009). The soil we used has a been classified as a sandy-skeletal, mixed, thermic Typic Torriorthent of the Arizo series (Soil Survey Division Staff, 1993) and is primarily vegetated with creosote bush [*Larrea tridentate* (DC.) Coville] and white bursage [*Ambrosia dumosa* (A. Gray) Payne].

Lysimeter Design and Instrumentation

The SEPHAS lysimeters are cylindrical, stainless steel tanks with a diameter of 226 cm and depth of 300 cm (Type 304, Moore's Blacksmith Shop) that are placed on truck scales (Model Z-100, Cardinal Scale Manufacturing Company) and housed underground in individual rooms that are accessible by a tunnel (Chief et al., 2009). Figure 1 shows a schematic diagram of the dimensions and design of the lysimeter. The scales have a resolution of 450 g and can detect changes in the lysimeter mass equivalent to a water column of 0.1 mm. The lysimeter tanks were filled with soil from bottom to top in individual lifts (between 2- and 22-cm lift thickness), with each individual lift being repacked as closely as possible to the bulk densities measured at the Eldorado Valley study site. The lysimeters have been kept free of vegetation since their installation in 2008. Chief et al. (2009) provides a comprehensive description of the three SEPHAS lysimeters.

Only the data from Lysimeter 1 are described here, since that lysimeter was the focus of our study. Lysimeter 1 has a homogenous texture profile with a fine fraction (<2 mm) consisting of 93.0% sand, 5.5% silt, and 1.5% clay and an average gravel content of 18.9% by mass. The lysimeter was repacked to the bulk density

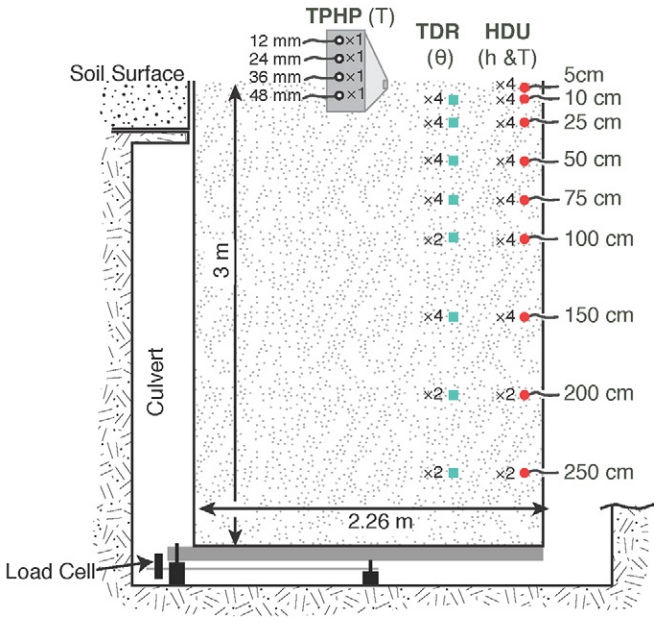

Fig. 1. Schematic diagram of lysimeter dimensions and the distribution of triple-probe heat probe (TPHP) sensors for temperature (T), time-domain reflectometry (TDR) sensors for water content (θ), and heat-dissipation unit (HDU) sensors for pressure head (h) and temperature (T). Numbers adjacent to the sensor icons indicate the number of replicates installed at each depth.

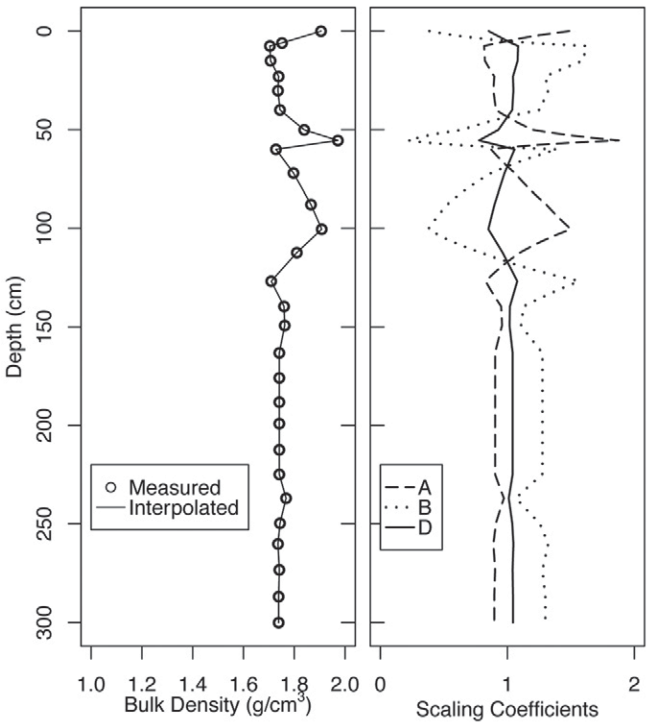

Fig. 2. Profile of the porosity (left panel) and corresponding linear scaling coefficients (right panel) of the water content (*D*), pressure head (*A*), and hydraulic conductivity (*B*).

profile shown in Fig. 2a, which reflects the bulk density profile of the undisturbed soil at the Eldorado Valley study site. Bulk densities ranged from 1442 to 1798 kg m^{-3}, yielding a porosity range from 0.24 to 0.31 (as calculated using an average measured particle density of 2479 kg m^{-3}).

Volumetric moisture contents were measured at depths of 10, 25, 50, 75, 100, 150, 200, and 250 cm using time-domain reflectometry (TDR) probes (Model CS605, Campbell Scientific). Four probes per depth were installed at 10, 25, 50, and 100 cm, and two probes per depth were installed at 75, 150, 200, and 250 cm. Soil water pressure heads (matric potentials) were monitored at depths of 5, 10, 25, 50, 75, 100, 150, 200, and 250 cm using heat dissipation units (HDUs; Model 229, Campbell Scientific). Four HDUs per depth were installed at 10, 25, 50, and 100 cm, and two HDUs per depth at 75, 150, 200, and 250 cm. Soil temperatures at depths of 5, 10, 25, 50, 75, 100, 150, 200, and 250 cm were determined using temperature sensors installed in the HDUs at the respective depths. Additionally, near-surface soil temperatures were measured at depths of 12, 24, 36, and 48 mm using triple-point heat dissipation probes (TPHP, East 30 Sensors). The arithmetic means of the soil water contents, pressure heads, and temperatures were calculated for each depth, and the averages were used for the various calculations.

Hourly precipitation and evaporation rates were calculated from lysimeter mass readings taken at 15-min intervals. Concurrently, precipitation rates were monitored using a tipping bucket rain gauge (Model TE525WS-L, Campbell Scientific) located ~30 m west of Lysimeter 1. The rain gauge provided precipitation data at 30-min intervals. This study covered the time period from 1 Oct. 2011 at 0000 h to 30 Sept. 2012 at 2300 h, which resulted in 8784 hourly measurements.

Laboratory Characterization of the Soil Water Retention Curve

The calibration range of the in situ pressure head sensors did not span the range that was experienced by the lysimeter soil. Additional laboratory measurements were performed using a dewpoint potentiometer (WP4, Decagon Devices) to provide data for calibrating the flow model in the dry range. Three disturbed and homogenized samples of the bulk soil were moistened to ~0.1 kg kg^{-1} and dried in consecutive steps by exposing them to the ambient laboratory environment for short intervals. After each drying interval, the samples were equilibrated overnight and their water potentials determined using the potentiometer, which was set in its manual mode to provide the most accurate readings. Gravimetric water contents were determined at each step using the sample mass, whereas the final mass was determined after oven drying at 105°C for 24 h. The gravimetric water contents were converted to volumetric fractions using the bulk density values of the pertinent soil layers in the lysimeter.

Model Description

One-dimensional unsaturated water flow and heat transport processes in the lysimeter were analyzed using the comprehensive HYDRUS-1D code, which has been successfully used to simulate vadose zone hydrologic processes of a wide range of soil and environmental problems (Šimůnek et al., 2016), including arid soil (Dixon, 1999). One major advantage of HYDRUS-1D for our study is its capability to simulate coupled heat and nonisothermal water flow in both the liquid and vapor phases. Nonisothermal liquid and vapor flow of water is described below as a sum of isothermal and non-isothermal components (Philip and de Vries, 1957; Saito et al., 2006):

$$\frac{\partial \theta_T(h)}{\partial t} = \frac{\partial}{\partial z}\left[\left(K + K_{vh}\right)\frac{\partial h}{\partial z} + \left(K_{LT} + K_{vT}\right)\frac{\partial T}{\partial z}\right] - S(h) \quad [1]$$

where $\theta_T = \theta + \theta_v$ [L^3 L^{-3}] is the total volumetric water content (i.e., the sum of the liquid and vapor components, respectively), with t being the time [T] and z being the soil depth [L]. The first part of Eq. [1] within brackets denotes the isothermal flux driven by pressure head (h [L]) gradients and includes liquid (K [L T^{-1}]) and vapor (K_{vh} [L T^{-1}]) phase fluxes. The second part represents water flow driven by thermal gradients (T [K]) and includes both liquid (K_{LT} [L^2 K^{-1} T^{-1}]) and vapor (K_{vT} [L^2 K^{-1} T^{-1}]) phase fluxes. The last term (S) of Eq. [1] denotes local sources and sinks. The accompanying heat transport equation is given by

$$C_p\theta\frac{\partial T}{\partial z}+L_0\frac{\partial \theta_v}{\partial z}= \frac{\partial}{\partial z}\left(\lambda\theta\frac{\partial T}{\partial z}-C_w q\frac{\partial T}{\partial z}-C_w\frac{\partial q_v T}{\partial z}-L_0\frac{\partial q_v}{\partial z}\right) \quad [2]$$

where C_p and C_w [M L^{-1} T^{-2} K^{-1}] are the volumetric heat capacities of the porous medium and the pore water, respectively; L_0 [M L^{-1} T^{-2}] is the heat of vaporization; λ is the effective thermal conductivity [M L T^{-3} K^{-1}]; and q and q_v (L T^{-1}) are the fluxes in liquid and vapor form. The flux terms are derived from the brackets in Eq. [1]. The thermal conductivity of the composite medium was calculated using an empirical relationship proposed by Chung and Horton (1987):

$$\lambda\theta=b_1+b_2\theta+b_3\theta^{0.5} \quad [3]$$

in which we used the parameter values b_1 = 0.228, b_2 = −2.406, and b_3 = 4.909, which are typical of a sandy texture, to yield λ in SI units [M L T^{-3} K^{-1}]. The water retention curve (WRC) of the porous medium was described using the dual-porosity model of Durner (1994):

$$S_e=(1-w)\left[1+(\alpha_1 h)^{n_1}\right]^{-m_1}+w\left[1+(\alpha_2 h)^{n_2}\right]^{-m_2} \quad [4]$$

where $S_e = (\theta - \theta_r)/(\theta_s - \theta_r)$ is effective saturation (with θ_s and θ_r representing the saturated and residual water contents, respectively), $m = 1 - 1/n$, and α [L^{-1}] and n are shape factors. The coefficients 1 and 2 in Eq. [4] represent distinct coarse and fine pore-size distributions, with the parameter w representing the fine pore-size distribution fraction. The isothermal liquid-phase hydraulic conductivity of the medium is then described using Mualem's (1976) approach (Durner, 1994; Priesack and Durner, 2006):

$$K=K_S\left[(1-w)S_{e1}+wS_{e2}\right]^l \times\left\{\frac{(1-w)\alpha_1\left[1-\left(1-S_{e1}^{1/m_1}\right)^{m_1}\right]}{(1-w)\alpha_1+w\alpha_2}+\frac{w\alpha_2\left[1-\left(1-S_{e2}^{1/m_2}\right)\right]^{m_2}}{(1-w)\alpha_1+w\alpha_2}\right\} \quad [5]$$

where K_S is the saturated hydraulic conductivity [L T^{-1}], and l is a pore-connectivity parameter (dimensionless). The thermal liquid-phase hydraulic conductivity is calculated by incorporating the temperature dependence of surface tension in Eq. [5]. This physically based formulation does not contain soil-specific parameters. Similarly, thermal and isothermal vapor conductivities are calculated by rewriting the thermal and isothermal vapor diffusivity equations (Saito et al., 2006).

The unsaturated hydraulic conductivity formulation given by Eq. [5] assumes that the soil pore system is made up of a bundle of capillaries. Although this assumption may be valid in the wet and intermediate range of the soil moisture spectrum (0.0 to −0.3 MPa), soil water dynamics in the lower extreme is dominated by adsorbed film flow, as well as vapor phase flow (Tuller and Or, 2001; Peters et al., 2015; Rudiyanto et al., 2015). Because water films sustain liquid flow at a higher rate than capillaries when the water content is very low, the unsaturated hydraulic conductivity at the lower end is likely always somewhat higher than what is predicted using Eq. [5]. Unfortunately, the contributions of film flow have not been widely adopted yet and are not included directly in the current version of HYDRUS-1D, unless they are accounted for indirectly by using dual-porosity hydraulic properties.

Parameterization of Soil Hydraulic Functions

Figure 2 shows that although the soil packed in the lysimeter has a uniform texture, the bulk density varies considerably. Representing this heterogeneity accurately in the model required partitioning the model domain into multiple layers, each with a distinct set of hydraulic parameters. This setup would result in an exorbitant number of free parameters and therefore cause the model to have very little interpretive value. To limit this problem, we treated the model domain as an equivalent homogenous medium with a single set of reference hydraulic parameters. Variability in the soil bulk density was accounted for by using a set of scaling parameters (Vogel et al., 1991) included in the HYDRUS-1D software. This allowed the water content, pressure head, and hydraulic conductivity at each node to be scaled independently by a set of depth-dependent coefficients. For this approach, it was also important to relate these coefficients to deviations of the bulk density from its reference value. In our analysis we used the depth of the shallowest set of sensors (0.1 m) as the reference depth. The derivations of the scaling relations are detailed in the Appendix. The final scaling coefficients for the water content, pressure head, and hydraulic conductivity were, respectively:

$$D_{XY}=\frac{\theta}{\theta^o}=\frac{\rho_b-\rho_s}{\rho_b^o-\rho_b} \quad [6]$$

$$A_{XY}=\frac{h}{h^o}=\left(\frac{\rho_b-\rho_s}{\rho_b^o-\rho_b}\right)^a \quad [7]$$

$$B_{XY}=\frac{K}{K^o}=\left(\frac{\rho_b-\rho_s}{\rho_b^o-\rho_b}\right)^b \quad [8]$$

where ρ_b is the soil bulk density (M/L^3), ρ_s is the particle density (M/L^3), and the superscript o is used to indicate values calculated using parameters corresponding to the reference depth (0.1 m). The coefficients a = −2.82 and b = −6.97 were determined by fitting Eq. [6–8] to water retention and hydraulic conductivity

data of granular porous media packed to different bulk densities (Laliberte et al., 1966).

To further reduce the number of free soil hydraulic parameters, the parameters of the WRC of the reference depth were determined by fitting the Durner model (Eq. [4]) to the measured water content and pressure head data. For the coarse pore-size fraction, we used data from the in situ water content and pressure head sensors at 0.1 m. For the fine pore-size fraction, which was assumed to be independent of packing density, we used the laboratory-measured water content and pressure head data. The lysimeter and laboratory data were used to determine the shape coefficients (α and n) of the two pore-size fractions and the weight of the finer pore-size fraction (w). The saturated water content (θ_s) was set to porosity, whereas the residual water content (θ_r) was assumed to be zero. These assumptions were made based on laboratory tests with lysimeter soil that was exposed to air having different relative humidity values between 0 (oven dried and then stored in a desiccator) and 80%. The corresponding volumetric water contents ranged from 0 to <1%.

In summary, the porosity and WRCs of the entire lysimeter were inferred from both in situ and laboratory measurements prior to the HYDRUS-1D simulations. We did not have any directly measured data that could be used to infer the saturated hydraulic conductivity and pore-connectivity coefficients. These were therefore determined by inverse modeling using HYDRUS-1D. The vapor hydraulic conductivity, as well as the thermal liquid-phase hydraulic conductivity coefficients, were calculated in HYDRUS-1D using physically based relations that did not require soil-specific parameters. The longitudinal thermal dispersivity was set at 0.00221 m (Hopmans et al., 2002). The thermal capacities of the mineral fraction and water were set to default values of $C_m = 2.49\ 10^5$ J m^{-3} K^{-1} and $C_w = 5.42\ 10^5$ J m^{-3} K^{-1}, respectively (Šimůnek et al., 2016).

Model Setup

In our study, we used HYDRUS-1D (V4.16.0110; Šimůnek et al., 2016) for all of the simulations. Our objective in using this model was twofold: to determine the saturated hydraulic conductivity using an inverse simulation, and to gain valuable insight into the main mechanisms governing surface fluxes and hydraulic redistribution processes within the lysimeter using a well-calibrated model.

The numerical model consisted of a 3-m-deep, single-material soil column that was uniformly discretized into 600 finite element layers of 0.005-m thickness. The variability in hydraulic properties due to variations in bulk density was mapped onto the flow domain using the scaling coefficients D_{XZ}, A_{XZ}, and B_{XZ} for the water content, pressure head, and hydraulic conductivity, respectively. The coefficients were first calculated separately for each lift of 0.1 m used during packing and subsequently interpolated linearly to obtain values for each layer. The coefficients of the first and last layers were extended to the top and bottom nodes of the numerical grid.

Initial Conditions

Initial conditions of the soil moisture content were obtained by interpolating moisture contents measured at the various depths on 1 Oct. 2011 at 0000 h. Because there were no sensors at the surface and bottom of the lysimeter, the values obtained from the highest and lowest sensors were extended to the top and bottom of the model domain, respectively. Initial soil temperature values were defined similarly, even though we had far more temperature sensors near the soil surface.

Boundary Conditions

The hydraulic top boundary condition was defined in terms of a time-dependent flux, which was calculated using the measured hourly changes in the lysimeter mass. This assumes that gains or losses in the lysimeter mass were caused only by precipitation or surface evaporation, respectively. The bottom boundary was set as a seepage face, which does not permit outflow when the boundary remains unsaturated. During the timeframe considered in this study, the wetting front had not yet arrived at the bottom of the lysimeter, which justified using these conditions. Lateral flow and lysimeter wall effects were not included in the one-dimensional model. Time-dependent temperature boundary conditions were imposed at the upper and lower boundaries as derived from the temperature measurements by TPHP sensors at 2.5 cm and a HDU sensor at 250 cm, respectively.

Calibration and Testing

The data used in this study started on 1 Oct. 2011 at 0000 h and ended a full year later on 30 Sept. 2012 at 0300 h, which resulted in 8784 hourly measurements. Two subsets of the data were used to separately calibrate and validate the model. An inverse simulation was conducted using a relatively wet subset of the data from Day 323 through Day 367 of the simulated time period (herein referred to as the water year). Hourly soil water contents from all eight depths were used for the inversion, which generated 4803 data points. Two versions of the inverse model were tested: one with both the saturated hydraulic conductivity (K_S) and the pore connectivity factor (l) as unknowns, and one with only K_S as unknown. The temperature data were not used for calibration. For the validation simulation, data from Day 0 to Day 125 were used. The model's goodness of fit was expressed in terms of the weighted RMSE and the coefficient of determination, R^2.

Results and Discussion

Water Retention Curves

The best-fit calibrated hydraulic conductivity (K_S) and pore connectivity parameter (l) are given in Table 1. Figure 3 shows measured and fitted WRCs for all depths. Water content and pressure head data pairs from the different in situ quadrants, as

Table 1. Best-fit calibrated parameters.

Description	Value
Fitted saturated hydraulic conductivity (K_S), cm h^{-1}	2.00
Pore connectivity parameter (l)	2.0
R^2	0.886
RMSE	6.223×10^{-5}

well as the laboratory samples, are represented by distinct symbols. Measurements outside the calibration ranges of the in situ pressure head sensors (-10^4 cm $\leq h \leq -10^2$ cm) and the laboratory WP4 potentiometer data ($h \leq -5 \times 10^4$ cm) were not included. The apparent hysteresis observed at 10 cm was thought to be due to a response time lag of the pressure head sensors. Additionally, the poor sensitivity of the in situ sensors near the upper limit of the calibration range did lead to an apparent asymptotic rise in measured water contents at pressure heads near −100 cm. However, because the exact thresholds of these biases were unknown, the Durner dual-porosity model was fitted to all measured data within the calibration range at a depth of 10 cm.

A nonlinear optimization code written in R (R Core Team, 2016) was used to fit the Durner model to the water retention data of the reference layer. Table 2 shows the best-fit Durner parameters of the lysimeter soil at a depth of 10 cm. Water retention parameters of the remaining layers were determined using Eq. [6–8] as described in the Appendix. Table 3 lists the corresponding scaling parameters. The dashed lines in Fig. 3 represent the fitted retention curves, and the solid lines represent the depth-adjusted WRCs. The differences in water retention between the layers can be attributed mostly to differences in bulk density (and therefore porosity), as shown in Fig. 2. Saturated water contents were set equal to the measured depth-specific porosities (i.e., $\theta_s = \phi$). We visually corroborated the scaled WRCs at all depths, but the goodness of fit was most obvious at depths of 25 to 75 cm.

Lysimeter Mass

Figure 4 shows the mass of Lysimeter 1 and the near-surface (6–12 mm) soil temperature data recorded during water year 2011. The temperature data clearly exhibited an annual cycle, with the range of the data points reflecting diurnal cycles. The lysimeter mass exhibited a continuous decline, which indicated evaporative losses, although there were occasional abrupt spikes during precipitation events. A change in lysimeter mass of 1 kg corresponded to a change in moisture depth of 0.25 mm. The observed range of changes in the water depth during the period of interest was ~63 mm.

Figure 5 shows the daily mass, vapor density, humidity, and temperature dynamics at four selected soil moisture periods. When the time series data were differentiated numerically to calculate lysimeter mass fluxes, small fluctuations (below the calibrated accuracy of the scale) were amplified. These fluctuations in the data were filtered using smoothed spline functions (R Core Team, 2016). We compared the original lysimeter mass data with the mass reconstructed by integration of the calculated flux to ensure that this smoothing did not alter the integrity of the data. Each period of the plots shown in Fig. 5 lasted 5 d. Figure 5 also shows the air temperature, relative humidity, and vapor density (measured 2 m above ground) values, as well as the near-surface soil temperature and lysimeter mass data. Two of the events represented relatively wet near-surface conditions (starting within 2 d after a rain event), whereas the other two events covered relatively dry conditions long after a rain event. The last two events were only 4 wk apart and separated by a period that had the largest rain event of the water year. The overall drying rate was more intense when the near-surface soil was still moist (1.2–1.5 kg d^{-1}) compared with the dry periods (~0.5 kg d^{-1}, approximately equal to the load-cell resolution).

A striking feature of Fig. 5 is the considerable diurnal mass fluctuation shown in the lower panel. One possible explanation for this periodicity is a thermal artifact of the weighing mechanism of the lysimeter. The diurnal temperature fluctuations of the near-surface soil (also plotted) were nearly identical at all times. A careful examination of the four intervals showed that the nighttime mass gains were more definitive (larger than the instrument resolution and less noisy) only when the surface soil was still wet. During these wet times, approximately half of the daily losses were regained during the night and early morning. In contrast, the mass gains (or fluctuations) during the dry times were very noisy. Additionally, the gain in mass started at or before midnight for wet soils when the soil surface was still cooling. This suggests that thermal artifacts on the performance of the scale do not fully explain the mass gain.

An alternative and more consequential explanation for the fluctuations is vapor condensation (dew) or direct vapor adsorption by the soil caused by large daily fluctuations in the surface-soil temperature (~30°C at 6–10 cm below the surface). The observed nighttime mass gains during the wet periods (~0.5 mm) are consistent with observations of nightly gains of soil water in the Negev Desert, which has a climate comparable with that of the Las Vegas area (Agam and Berliner, 2004; Hill et al., 2015). The above considerations justify including the mass gain as a surficial deposition of moisture.

Model Calibration

The subset of data from water year 2011–2012 used for model calibration is indicated by the shaded region in Fig. 4, marked as "Cal." This subset commenced when the lysimeter was the lightest (driest) during the year and contains data from three major storms, including the largest storm of the year (which added >50 mm in precipitation). Figure 6 compares the measured and best-fit modeled cumulative mass fluxes across the lysimeter surface. Because mass losses through all surfaces of the lysimeter other than the soil surface were considered negligible, the cumulative mass flux should be equivalent to the net mass change from the

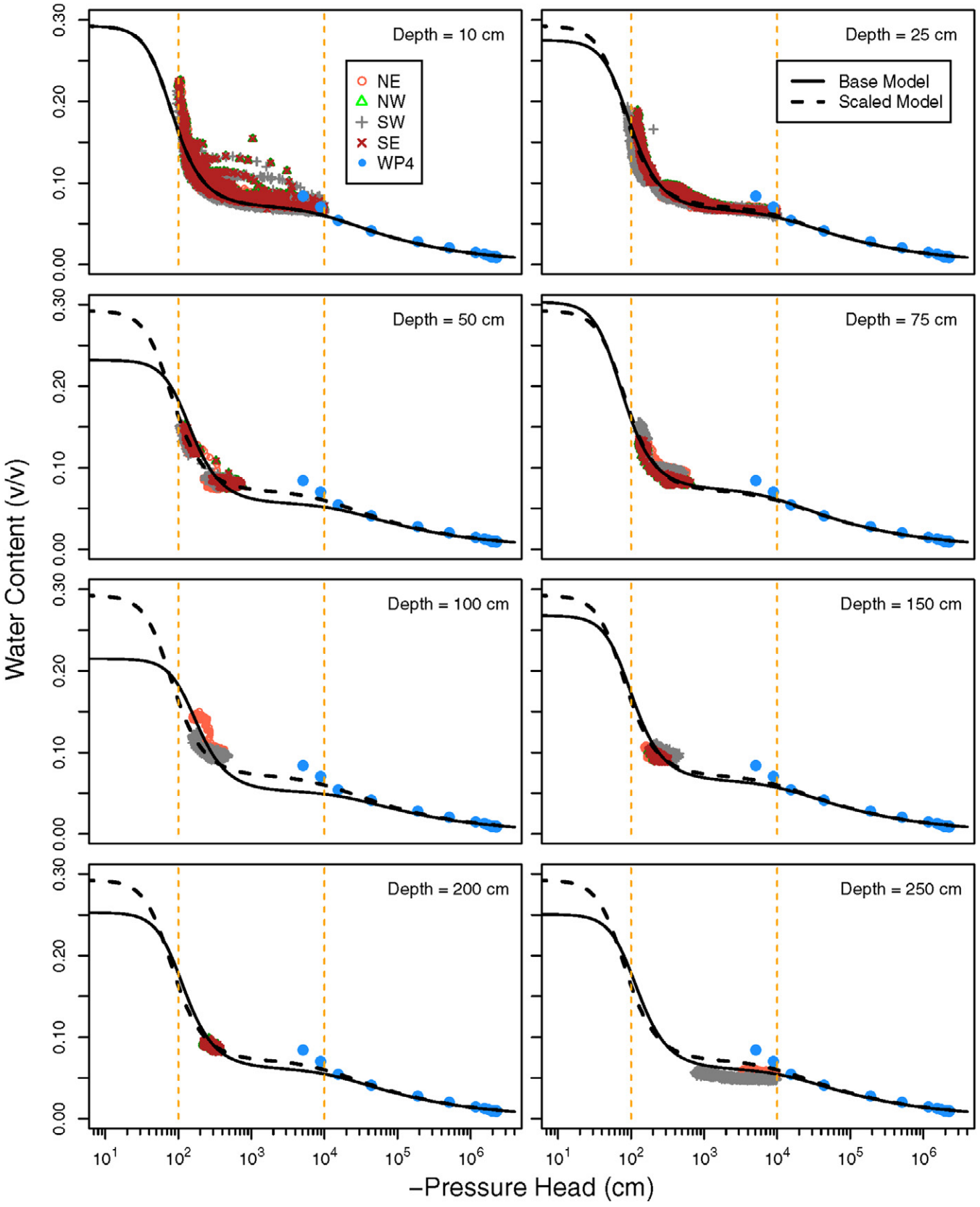

Fig. 3. Water retention curves of the lysimeter soil at various depths. The symbols correspond to water contents and pressure heads measured at the corresponding depths and quadrants (NE, northeast; NW, northwest; SW, southwest; SE, southeast) or laboratory data derived from dew-point potentiometer (WP4) measurements. The dashed lines represent the Durner's dual-porosity model fitted to the 10-cm data, and the solid lines are curves transformed using linear scaling coefficients.

Table 2. Directly determined hydraulic parameters of the lysimeter soil layer at the 10-cm depth.

Parameter	Value
Saturated water content (θ_s)	0.292
Residual water content (θ_r)	0.000
Durner parameter α_1 (coarse subcurve), cm^{-1}	1.57×10^{-2}
Durner parameter n_1 (coarse subcurve)	2.571
Durner parameter α_2 (fine subcurve), cm^{-1}	10^{-4}
Durner parameter n_2 (fine subcurve)	1.35
Fraction of fine subcurve (w)	0.245

start of the calibration period. The model generally captured the infiltration and evaporation dynamics well. However, the simulated rate of drying was slower than the observations. This discrepancy increased over time, which led to the widening gap shown in Fig. 6. Dixon (1999) found similar results comparing measured with HYDRUS-1D-simulated soil water storage in the bare soil of a weighing lysimeter at the Nevada Test Site in Nye County, Nevada.

Figure 7 shows a comparison of measured and simulated water contents of all eight observation layers. Only the water content data were used in the calibration. The reported error bands are standard measurement errors from the four lysimeter quadrants, except for the data at depths of 100, 200, and 250 cm, which each had only two sensors. In general, the model accurately captured the observed water content dynamics in the top 1 m of the lysimeter, except for two distinct discrepancies. One discrepancy occurred during the late stages of drying at 10 cm, where the simulated rate of drying lagged behind the measured rate. This lag is consistent with the discrepancy in the surface mass flux noted earlier. The other discrepancy occurred when the wetting front reached 75 cm. The standard error of the water content at 75 cm (according to the TDR sensors at the four quadrants) showed an abrupt increase at the same time. A closer inspection of the data from individual

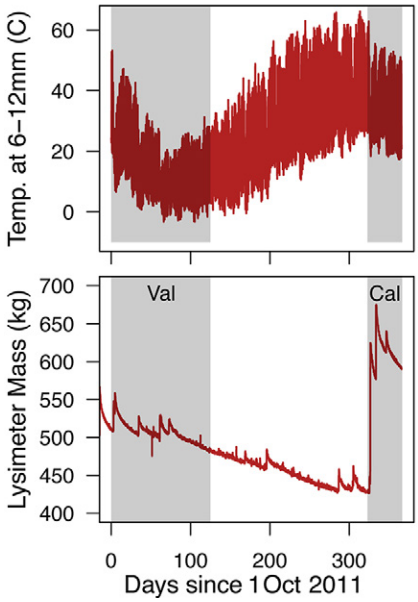

Fig. 4. Temperatures of the near-surface lysimeter soil and validated (Val.) and calibrated (Cal.) total mass of the lysimeter during water year 2011–2012.

quadrants (data not shown) revealed that the northwest quadrant was slightly drier than the other locations at and below 75 cm. This suggests that a preferential flow path may have developed at that depth. At 100 cm, which had sensors only in the northeast and southwest quadrants, the arrival of the wetting front was much slower. Incomplete contact between the sensor and the soil may have been another reason for the differences in moisture contents measured at 75-cm depth. Although the sensors were carefully installed in the disturbed soil, incomplete sensor-to-soil contact cannot be ruled out. Below 1 m, no changes in the moisture content were observed in the water year 2011–2012.

Figure 8 shows a comparison of measured and simulated temperatures of the eight observation layers. The temperature datasets were not used to calibrate the model, which confirms that the

Table 3. Fitted scaling parameters for the remaining depths.

	Fitted scaling parameter†					
Depth	Bulk density	Porosity	$(\rho_b' - \rho_s)/(\rho_b - \rho_s)$	D_{XY}	A_{XY}	B_{XY}
cm	$g\ cm^{-3}$					
10	1.70	0.292	1.000	1.000	1.000	1.000
25	1.74	0.275	0.941	0.941	1.165	0.693
50	1.84	0.232	0.793	0.793	1.785	0.249
75	1.64	0.303	1.037	1.037	0.913	1.244
100	1.91	0.215	0.735	0.735	2.159	0.158
150	1.76	0.268	0.916	0.916	1.245	0.591
200	1.74	0.253	0.864	0.864	1.440	0.417
250	1.74	0.251	0.857	0.857	1.471	0.396

† ρ_b', bulk density; ρ_s, particle density; D_{XY}, linear scaling coefficient of water content; A_{XY}, linear scaling coefficient of pressure head; B_{XY}, linear scaling coefficient of hydraulic conductivity.

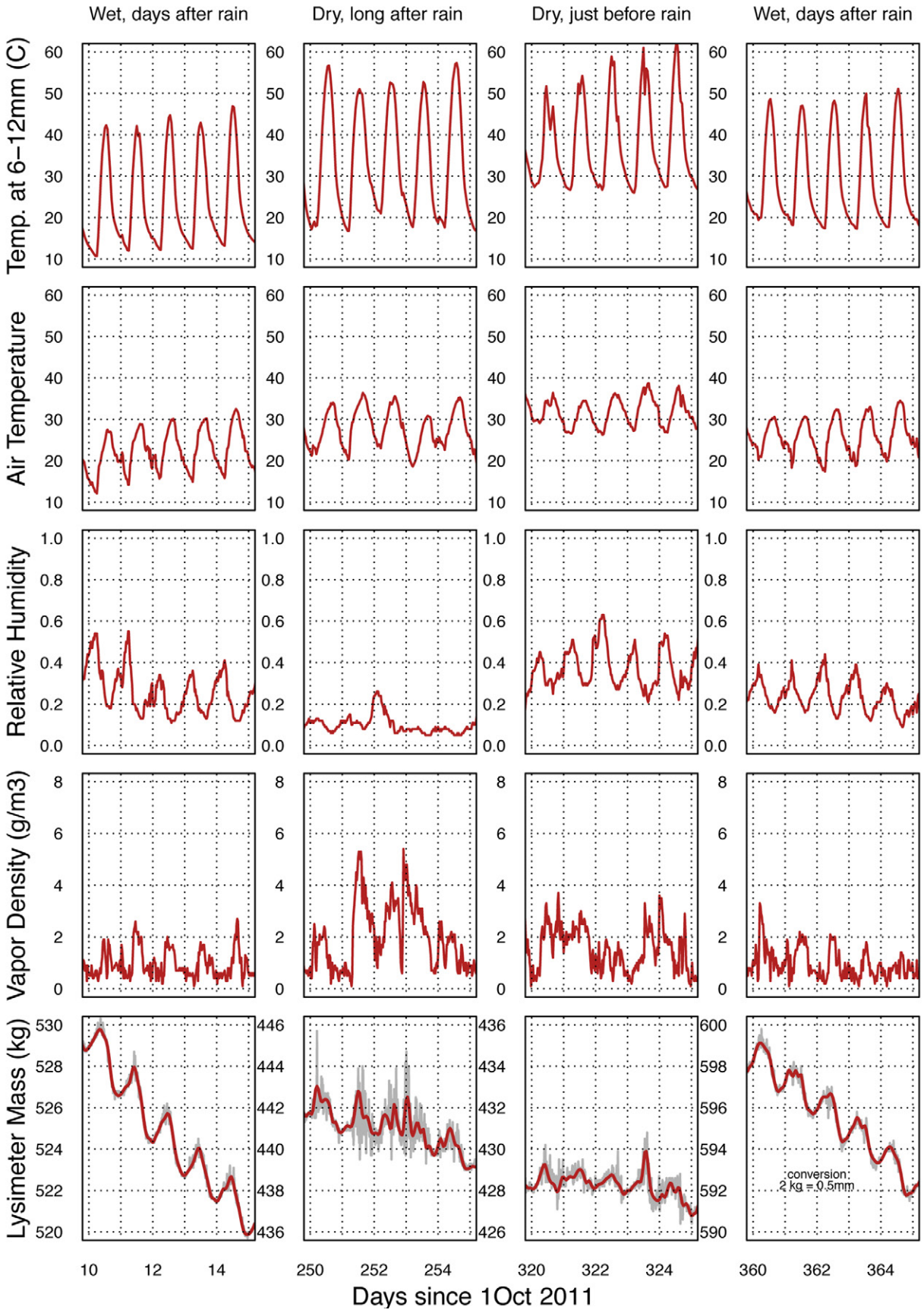

Fig. 5. Diurnal dynamics of near-surface soil temperature, air temperature, air relative humidity, air vapor density, and lysimeter mass data during four periods when the surface soil was wet and dry.

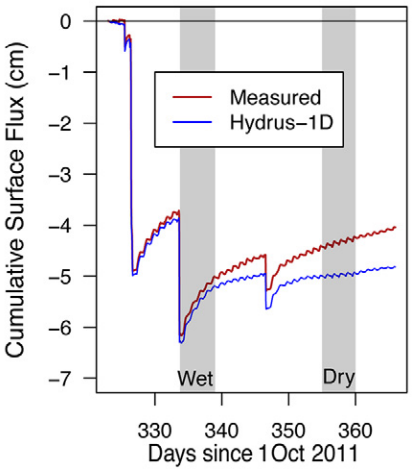

Fig. 6. Measured cumulative mass fluxes, assuming that lysimeter mass changes were due to water fluxes through the upper boundary only, and corresponding best-fit modeled mass fluxes during the calibration period.

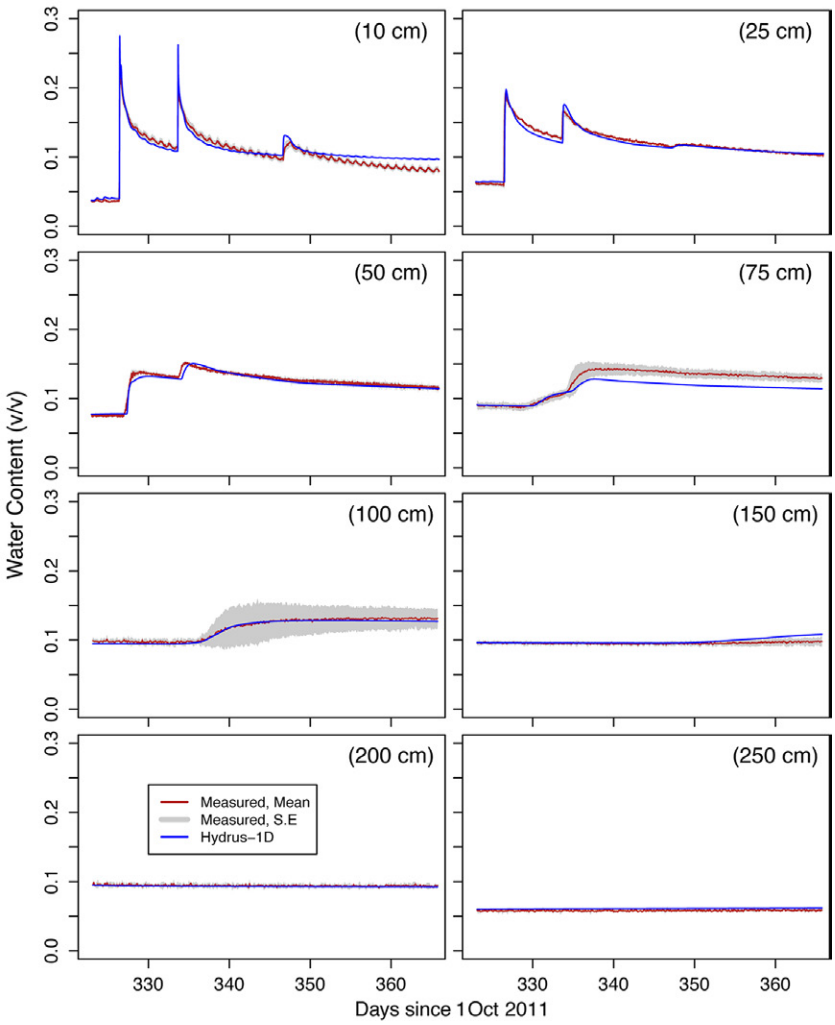

Fig. 7. Measured and modeled water contents at eight layers during the calibration period. The shaded regions represent standard errors (SE) of four replicate sensors except at 100, 200, and 250 cm, where they denote the range of two sensors.

thermal properties of the soil were set a priori. The model captured the temperature dynamics in the top 25 cm accurately, but the results deviated from the measurements starting at 50 cm. The deviations were probably caused by variations in soil bulk density (and therefore thermal properties) with depth, with the most notable variability occurring in the 40- to 120-cm region (Fig. 2). However, the solid fraction in the model was kept uniform (set to the value corresponding to the porosity at 10-cm depth), since HYDRUS-1D does not permit any scaling of thermal properties. The discrepancy thus appears to be caused by inconsistent thermal properties. The discrepancies at 50 and 100 cm are propagated by the model to the underlying layers.

Discrepancy and Diurnal Fluctuations

To better understand the main causes of the discrepancy between the simulated and observed drying rates, we examined the simulated surface pressure heads, as well as the simulated and measured surface mass fluxes at two 5-d intervals during the calibration period (Fig. 9). The first interval started immediately before the second rain event (Day 333) and included the wettest period of water year 2011–2012. The second interval occurred during a dry spell at the end of the calibration period. During the first 3 d of the wet period (Fig. 9a), the surface soil remained fairly wet, and the simulated and measured surface mass fluxes were essentially identical. However, when the soil surface began to dry significantly, reaching a pressure head minimum of -10^6 cm (air-dry conditions), the model was not able to reproduce the measured flux (see the afternoon of Day 338). During the dry period (Fig. 9b), the surface soil remained fairly dry (especially in the afternoons), and the model consistently failed to match the observed upward fluxes. The accumulation of these daily discrepancies resulted in deviations between the observed and modeled cumulative mass fluxes as shown in Fig. 6.

The above discrepancies suggest that the nonisothermal flow processes as described by the extended Richards equation (Eq. [1]) do not fully represent the high drying rates when the surface soil was at or near air-dry conditions. To better understand the flow dynamics during times when the model failed to capture the observed drying rates, we examined the vapor and liquid fluxes in the top 100 cm on Days 336 and 357, respectively. These dates are in the middle of the wet and dry periods. The dashed lines in the top plot of Fig. 10 represent the points in time at which the fluxes were calculated. Overall, vapor flow played a minor role compared with the liquid flux. A significant vapor flux occurred only during the second half

of the wet day and was limited to the top few centimeters. During the relatively dry Day 357, a downward flux was observed during the first half of the day, with the total flux being divided almost equally between the vapor and liquid fluxes. However, in the afternoon of Day 357, just when the model started to fail in capturing the observed flux, the upward flux was driven only by liquid water flow that mostly originated from the top few centimeters. No upward flux occurred below 5 cm. The model thus failed to fully capture the drying process, since there was no sufficient liquid flux. Additionally, the surface soil reached a pressure head of -10^{-6} cm at this time (Fig. 9, top). These results are consistent with the basic premises of the van Genuchten–Mualem model (Mualem, 1976; van Genuchten, 1980) of unsaturated hydraulic conductivity. When the soil is in such a dry state, a very strong gradient in the pressure head cannot overcome the steep drop in the hydraulic conductivity.

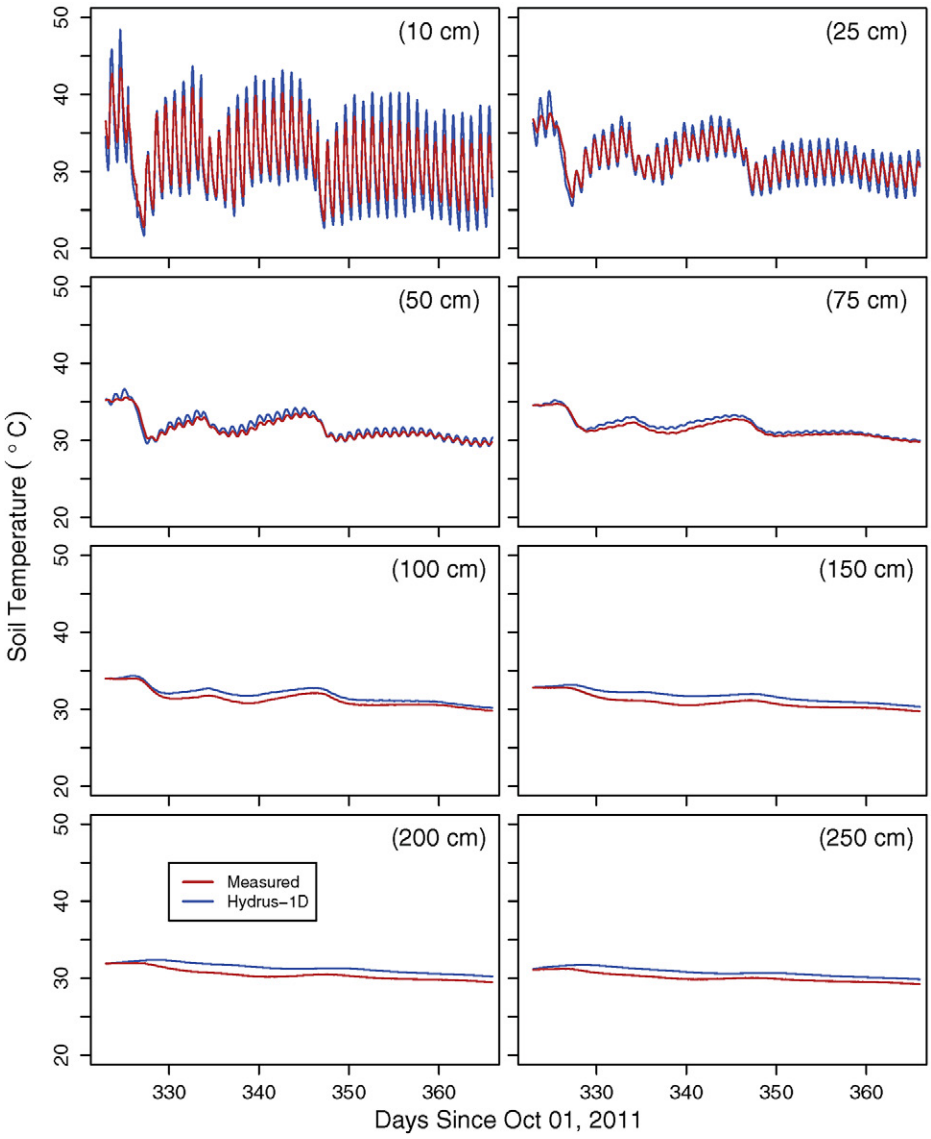

Fig. 8. Measured and simulated temperatures at eight layers during the calibration period. The shaded regions represent the standard errors of four replicate sensors except at 200 and 250 cm, where they denote the range of two sensors.

Validation Period

Figure 11 shows a comparison of measured and best-fit simulated cumulative mass fluxes at the lysimeter surface. The validation period was marked by four low-intensity rain events, which added a total of ~5 m of precipitation to the lysimeter. However, the lysimeter recorded a net loss of ~0.6 cm through the validation period. The wetting front from the rain events clearly registered at 10 cm and showed very small and slow increases at 25 cm (Fig. 12), which indicates that most or all of the rainwater had been lost by evaporation and not deep drainage. The model accurately predicted the wetting dynamics during all four rain events but failed to fully capture the drying dynamics. This discrepancy between the model predictions and the measurements increased during the slow but steady drying process that followed the rainfall events.

In comparison, HYDRUS-1D predicted the temperature dynamics at all depths reasonably well, as shown by the results in Fig. 13. The predicted temperature dynamics exhibited wider diurnal fluctuations than the sensor data at 10 and 25 cm. However, there was no lateral variability in the recorded temperatures, which is evident by the nearly invisible error margins.

Model Limitations and the Way Forward

Evaporation from initially wet, bare porous media is typically divided into three distinct stages (Idso et al., 1974; Or et al., 2013). The first two stages—commonly referred to as Stage I, or the constant rate period, and Stage II, or the transition period—are controlled by the evaporative demand of the ambient atmosphere and last as long as there is a continuous liquid water supply to the surface facilitated by upward capillary flow (Or et al., 2013). The transition from Stage I to Stage II evaporation represents the transition from saturated or near-saturated flow to increasingly unsaturated upward flow at rates that are less that the potential evaporation rate. The phase transition of water from liquid to vapor during Stages I and II mostly occurs at the soil surface, and this process controls the actual evaporation rate. In this regard,

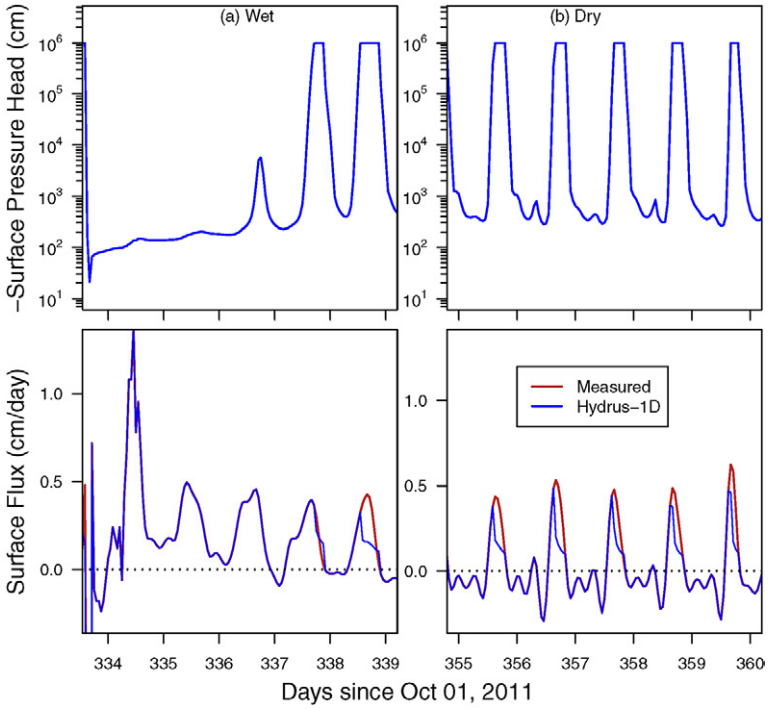

Fig. 9. Modeled surface pressure head and prescribed and actual modeled surface fluxes of water during (a) wet and (b) dry periods. HYDRUS-1D could not model the prescribed flux when the surface soil was very dry.

HYDRUS-1D and the underlying Richards equation satisfactorily capture subsurface liquid water flow. This is evident in the comparisons between the simulated and measured mass losses over the few days immediately after each rain event, during both the calibration and validation periods (Fig. 6 and 11).

During Stage II, liquid water flow to the surface occurs under increasingly unsaturated conditions to meet the evaporative demand at the surface. When the rate of water supply is no longer adequate to match the evaporative demand, even with increasingly steeper pressure head gradients near the soil surface, the continuous stream of liquid water that supplies the evaporating surface breaks and a dry soil layer forms at the surface. This results in a further drop in the evaporation rate and marks the transition from Stage II to Stage III evaporation. Stage III evaporation is controlled by water vapor diffusion through the dry layer above the secondary drying front (Shokri et al., 2008), where phase changes occur at and below the soil surface. As the secondary drying front recedes deeper into the soil, the length of the diffusive path increases, which leads to a continuous decrease in the overall evaporation rate. The drop in the evaporation rate during

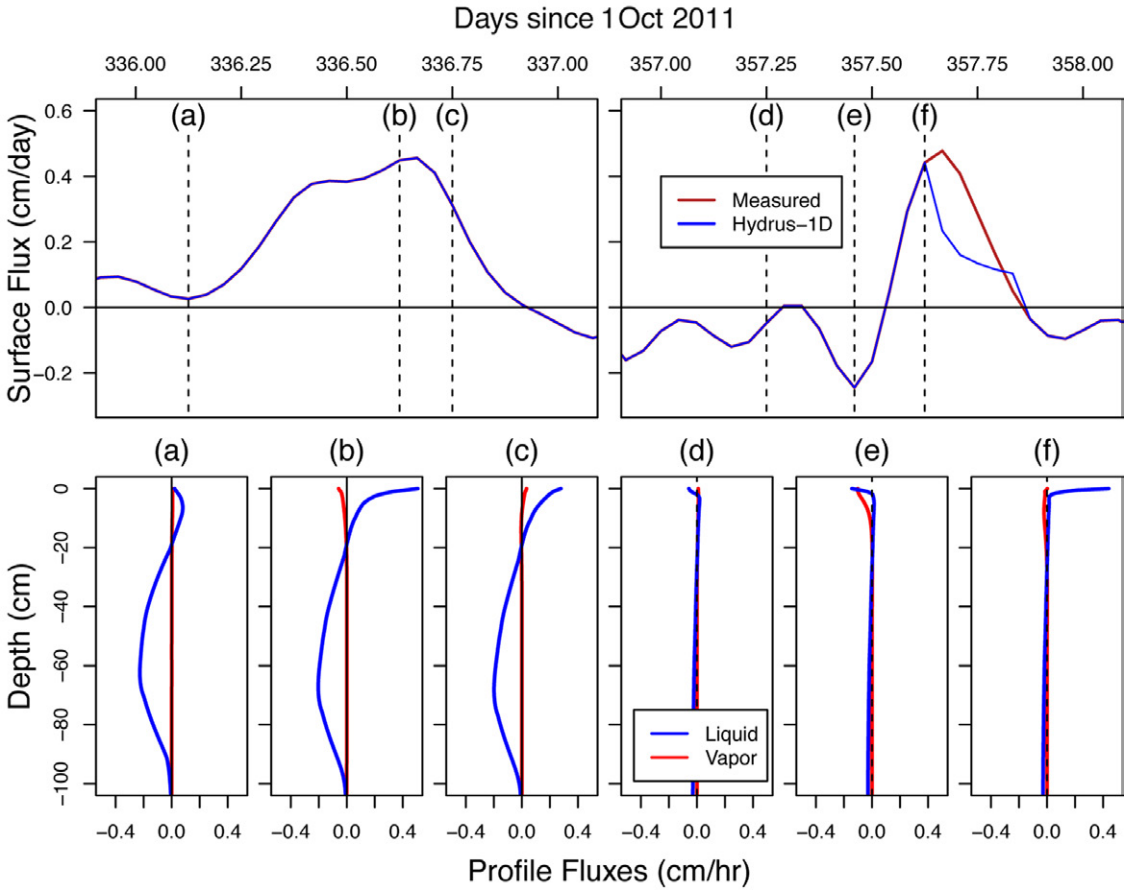

Fig. 10. Prescribed and actual simulated surface fluxes of water during wet (left) and dry (right) days and liquid- and vapor-phase fluxes in the top 100 cm at selected times. The dashed lines represent the points in time at which the fluxes were calculated.

the transition between Stages II and III depends on the depth of the drying front when the liquid-phase discontinuity first emerges and a secondary drying front forms (Shokri et al., 2008). Lehmann et al. (2008) suggested that this depth is a characteristic property of the porous medium that depends on the pore-size distribution of the medium. Shokri and Or (2011) estimated values between 3 and 14 mm (depending on the soil texture, ranging from coarse to very fine) as the initial thickness of the dry layer and the initial depth of the secondary drying front.

The results of our study highlighted two inherent limitations of the governing equations (Eq. [1–5]) underlying HYDRUS-1D and similar simulators. One limitation is that although the model accounts for nonisothermal vapor diffusion (see Eq. [1]), it does not permit discontinuity in the liquid phase. Therefore, the vapor pressure is assumed to be in equilibrium with a continuous but increasingly drier matrix during Stage III. This assumption limits the vapor concentration gradient that can be established between the drying front and the surface. Model limitations associated with this shortcoming can only be alleviated by enabling liquid-phase discontinuities with a moving boundary within the model domain, such as using a secondary drying front as proposed by Shokri et al. (2008). This forced continuity leads to a pressure head that asymptotically tends toward infinity near a drying soil surface. To avoid numerical instability and thermodynamically unrealistic pressure head values, HYDRUS-1D imposes a minimum pressure head. In this study, we used a value of $h_{crit} = -10^6$ cm, which corresponds to typical air-dry conditions (the model results were not sensitive to variations in the range -10^8 cm $< h_{crit} < -10^6$ cm). The bimodal Durner WRC afforded adequate flexibility that matched the measured behavior in the hyper-dry and wet regimes.

The other limitation is that the underlying assumption behind Mualem's model of the unsaturated hydraulic conductivity does not adequately describe flow in the hyper-dry regime. The model was derived assuming that the porous medium can be approximated by a bundle of capillary tubes. This conceptualization adequately describes the retention and dynamics of capillary menisci in wet and moderately wet systems but does not represent the soil water dynamics well when soil water is distributed in the form of thin films. The discrepancy is particularly noticeable when simulating liquid flow. The

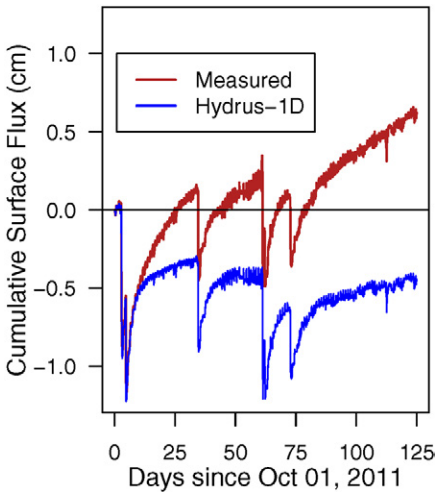

Fig. 11. Measured cumulative mass fluxes, assuming that lysimeter mass changes were caused by water fluxes across the upper boundary only, and corresponding predicted mass fluxes during the validation period.

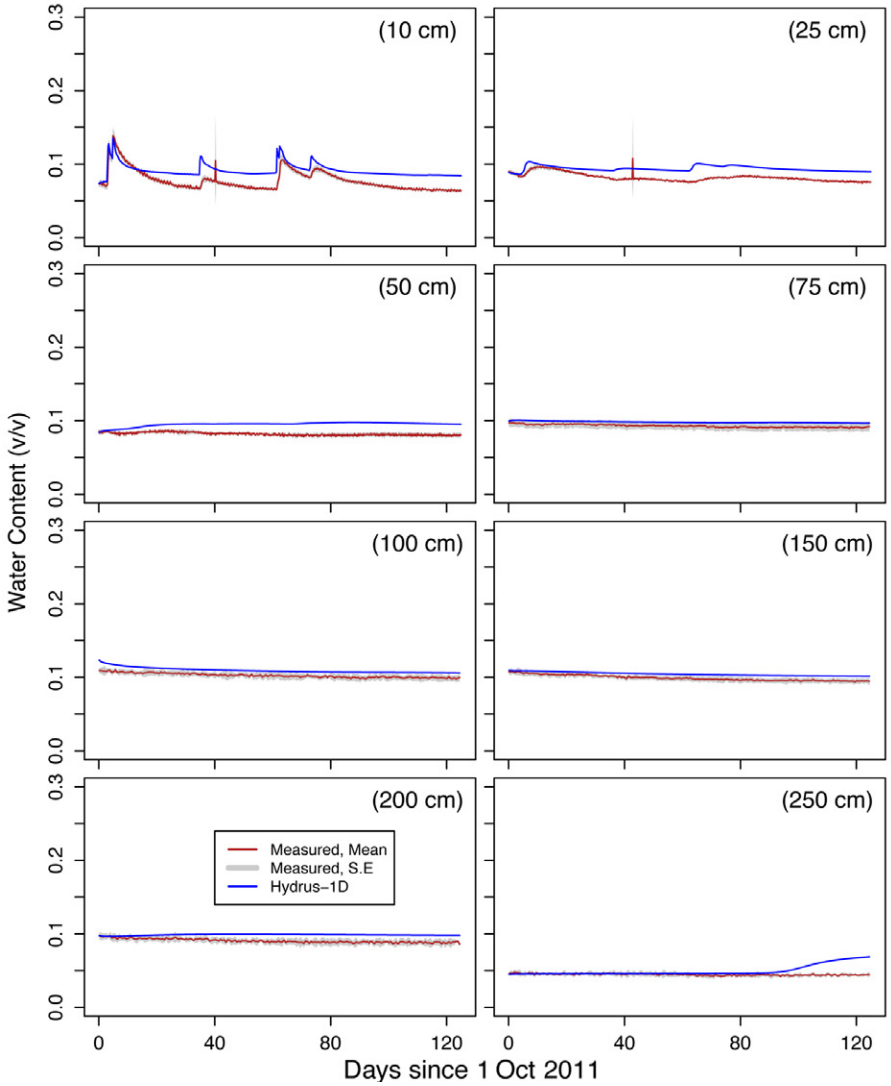

Fig. 12. Measured and predicted water contents at eight layers during the validation period. The shaded regions represent standard errors of four replicate sensors except at 200 and 250 cm, where they denote the range of two sensors.

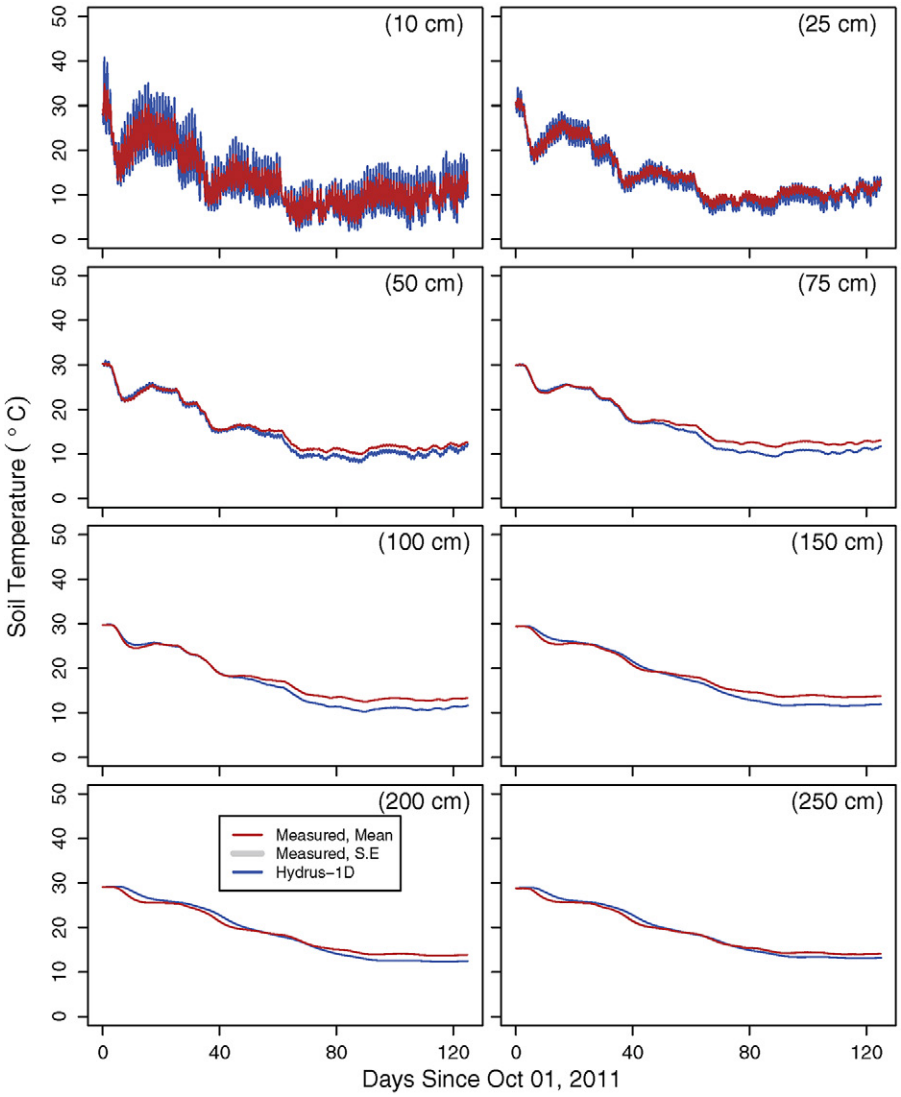

Fig. 13. Measured and modeled temperatures at eight layers during the validation period. The shaded regions represent the standard error of four replicate sensors except at 200 and 250 cm, where they denote the range of two sensors.

bundle-of-capillaries assumption requires the unsaturated hydraulic conductivity to drop indefinitely at a steep rate with lower negative pressure heads. However, conceptual models of unsaturated flow that integrate both capillary and film flow (Tuller and Or, 2001) show that the decline in hydraulic conductivity with decreasing pressure heads is more tapered. This problem can be addressed by using unsaturated hydraulic conductivity functions that integrate capillary and film flow and possibly vapor flow (Tuller and Or, 2001; Peters et al., 2015; Rudiyanto et al., 2015).

The discrepancy between simulated and measured evaporation rates in this study is likely related to both of the above limitations (i.e., properly accounting for evaporation from moving boundaries away from the soil surface and accounting for film flow). The high-quality, long-term data available from the SEPHAS lysimeter facility provide a compelling opportunity to address this critical gap in modeling soil moisture dynamics and evaporation in very dry soils. A model that can capture all of the infiltration, redistribution, and evaporation processes of water in arid soils will be a valuable tool for quantifying the moisture dynamics of arid ecosystems and their effects on climate change, plant growth, erosion, and recharge patterns.

Conclusions

The SEPHAS lysimeter facility provides a unique dataset for desert hydrologic research. The lysimeters are instrumented with reliable and accurate sensors with robust quality control and curating mechanisms in place. The well-defined upper boundary condition and the accurate scale allowed us to close the water balance. Additionally, the high density of data acquisition allowed for a reliable representation of water flow in unsaturated desert soil.

In this study, we tested the reliability of the conventional approaches of modeling unsaturated flow in the dry end of the soil water spectrum. We showed that infiltration and redistribution could be represented fairly accurately with the Richards equation. The model also performed well in describing the early stages of evaporation (i.e., Stage I and parts of Stage II evaporation), when the evaporative demand at the soil surface is the primary driver. However, the model consistently underestimated Stage III evaporation. We identified two potential causes that contributed to this discrepancy. First, the classical Richards equation does not permit hydraulic discontinuity and vapor-diffusion-limited water transfer from a subsurface drying (evaporation) front upward to the soil surface. The forced continuity requires unrealistic equilibration between an extremely dry but continuous thread of liquid water and vapor. Vapor flow that occurs under such conditions is likely to underestimate Stage III evaporation. Second, the hydraulic conductivity model used in the HYDRUS-1D code likely underestimates water flow rates for very dry soil conditions. More work is clearly needed to delineate the relative contributions of these two shortcomings and to correct for their effects.

Appendix: Linear Scaling of Hydraulic Properties

The variability in bulk density in the lysimeter was accounted for in the simulations by using scaling coefficients. Water contents,

pressure heads, and hydraulic conductivities at each node can be independently scaled by coefficients in HYDRUS-1D. The approach permits one to consider the profile as a homogeneous medium using parameters of the reference state, but with adjustments for each separate soil layer using the three coefficients.

Consider the WRC of a soil at a reference bulk density (van Genuchten, 1980):

$$\theta = \theta_r + (\theta_s - \theta_r)\left[1 + (\alpha h)^n\right]^{-m} \quad [A1]$$

where $\theta_s = \phi_{max}$. Similarly, the WRC of the same soil but at different bulk density can be written as:

$$\theta' = \theta'_r + (\theta'_s - \theta'_r)\left[1 + (\alpha' h')^{n'}\right]^{-m'} \quad [A2]$$

Equation [A1] represents the reference state and Eq. [A2] the altered state. Following Vogel et al. (1991), the dimensionless scaling rules that are permitted in HYDRUS-1D are

$$\frac{\theta' - \theta'_r}{\theta - \theta_r} = D_{XZ} \quad [A3]$$

$$\frac{h'}{h} = A_{XZ} \quad [A4]$$

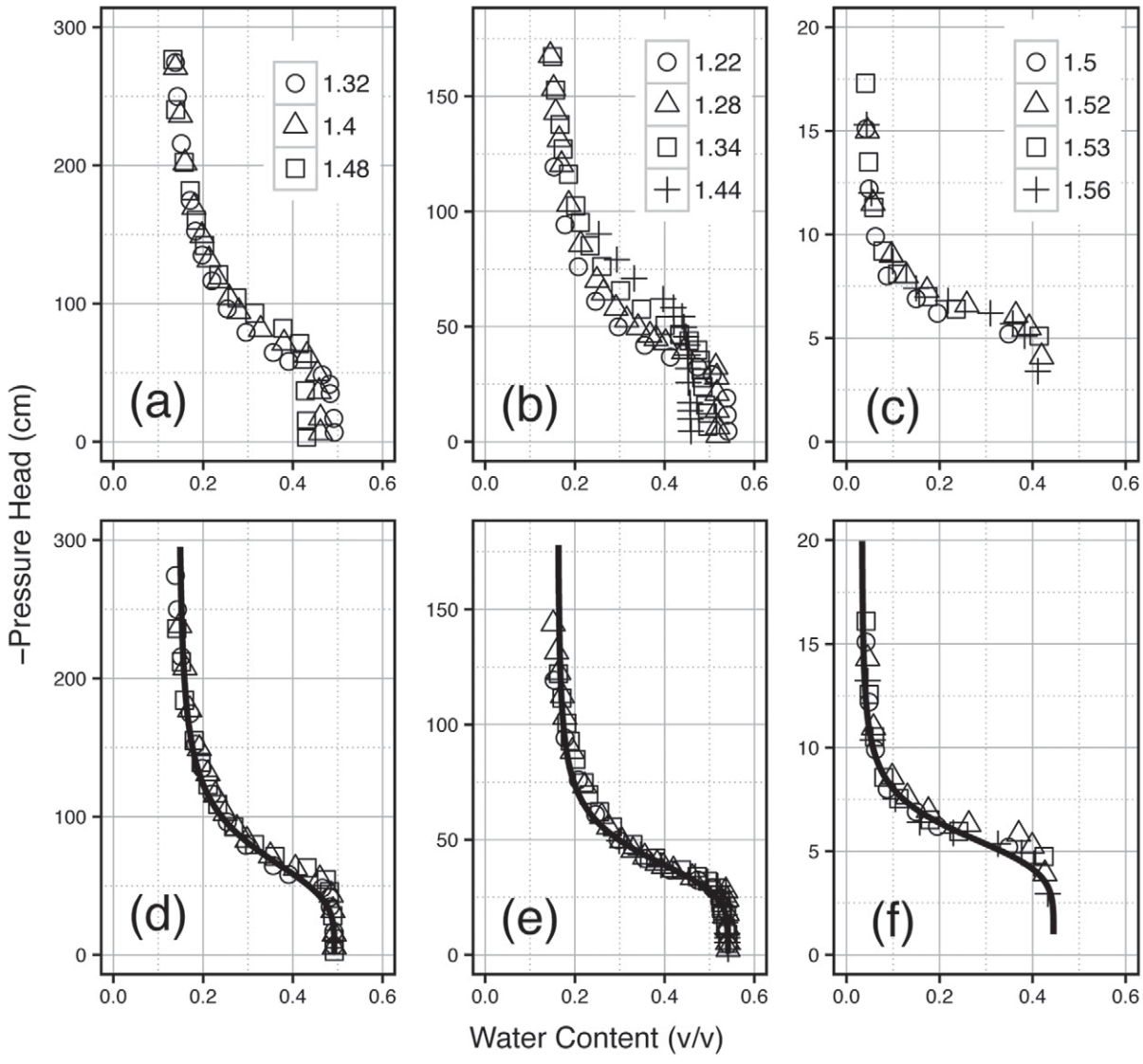

Fig. A1. Water retention curves of (a,d) Touchet silt loam, (b,e) Columbia sandy loam, and (c,f) unconsolidated sand packed to varying degrees of bulk density. Original data derived from Laliberte et al. (1966) are in the top row. Water contents and pressure heads were rescaled by the bulk density according to the proposed formulation (bottom row). The solid lines represent van Genuchten water retention fits to the lowest bulk density sample of each soil.

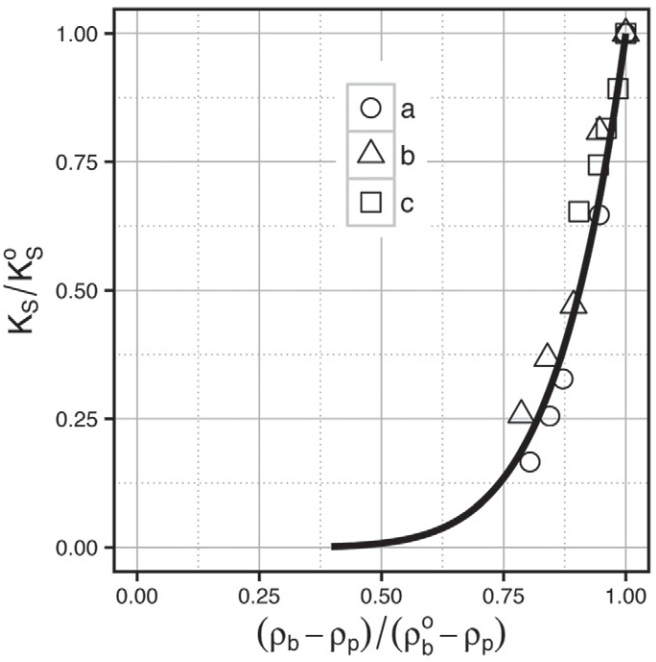

Fig. A2. Saturated hydraulic conductivity (K_S) of (a) Touchet silt loam, (b) Columbia sandy loam, and (c) unconsolidated sand packed to varying degrees of bulk density (ρ_b) derived from Laliberte et al. (1966). The solid line represents the proposed scaling relation. The superscript o is used to indicate values calculated using parameters corresponding to the reference depth (0.1 m).

$$\frac{K_S'}{K_S} = B_{XZ} \qquad [A5]$$

Substituting Eq. [A3] and [A4] in Eq. [A1] and comparing the result with Eq. [A2] leads to

$$D_{XY} = \frac{\rho_b' - \rho_s'}{\rho_b - \rho_s} \qquad [A6]$$

This shows that we can then use a power-law relation to describe the other two scale factors:

$$A_{XY} = \left(\frac{\rho_b' - \rho_s}{\rho_b - \rho_s}\right)^a \qquad [A7]$$

$$B_{XY} = \left(\frac{\rho_b' - \rho_s}{\rho_b - \rho_s}\right)^b \qquad [A8]$$

Therefore, what remains to be found are the appropriate values of *a* and *b*. A similar approach was used by Assouline et al. (1997).

Figure A1 shows how Eq. [A6] and [A7] can be used to rescale the WRC of compacted soils (top row) to match the uncompacted WRC (bottom row). The data correspond to variably packed columns of Touchet silt loam (coarse-silty, mixed, superactive, mesic Cumulic Haploxerolls), Columbia sandy loam (coarse-loamy, mixed, superactive, nonacid, thermic Oxyaquic Xerofluvents), and unconsolidated sand (Laliberte et al., 1966). The best-fit value of *a* was found to be –2.83. Similarly, Fig. A2 shows scaled K_S values vs. porosity data for all three soils. The data exhibit consistent scaling with a best-fit value of 6.97 for *b*. The two scaling coefficients *a* and *b* consistently worked well for the three granular media and were assumed to be applicable to the SEPHAS lysimeter as well.

Acknowledgments

This paper is based on work supported by the US National Science Foundation under Grants no. IIA-1301726 and EPS-0447416, as well as grants from the Desert Research Institute's Division of Hydrologic Sciences International Student Program and the Royal Dutch Institute for Engineers (KIVI NIRIA). We are grateful to Ms. Nicole Damon for carefully editing the manuscript, as well as Dr. Markus Flury and three anonymous reviewers for their valuable comments and suggestions.

References

Agam, N., and P.R. Berliner. 2004. Diurnal water content changes in the bare soil of a coastal desert. J. Hydrometeorol. 5:922–933. doi:10.1175/1525-7541(2004)005<0922:DWCCIT>2.0.CO;2

Andraski, B.J. 1997. Soil-water movement under natural-site and waste-site conditions: A multiple-year field study in the Mojave Desert, Nevada. Water Resour. Res. 33:1901–1916. doi:10.1029/97WR01502

Andraski, B.J., W.A. Jackson, T.L. Welborn, J.K. Bohlke, R. Sevanthi, and D.A. Stonestrom. 2014. Soil, plant, and terrain effects on natural perchlorate distribution in a desert landscape. J. Environ. Qual. 43:980–994. doi:10.2134/jeq2013.11.0453

Assouline, S., J. Tavares, and D. Tessier. 1997. Effect of compaction on soil physical and hydraulic properties: Experimental results and modeling. Soil Sci. Soc. Am. J. 61:390–398. doi:10.2136/sssaj1997.03615995006100020005x

Austin, A.T., L. Yahdjian, J.M. Stark, J. Belnap, A. Porporato, U. Norton, et al. 2004. Water pulses and biogeochemical cycles in arid and semiarid ecosystems. Oecologia 141:221–235. doi:10.1007/s00442-004-1519-1

Bhattachan, A., P. D'Odorico, M.C. Baddock, T.M. Zobeck, G.S. Okin, and N. Cassar. 2012. The Southern Kalahari: A potential new dust source in the Southern Hemisphere? Environ. Res. Lett. 7:024001. doi:10.1088/1748-9326/7/2/024001

Chief, K., M.H. Young, B.F. Lyles, J. Healey, J. Koonce, E. Knight et al. 2009. Scaling environmental processes in heterogeneous arid soils: Construction of large weighing lysimeter facility. Desert Res. Inst., Las Vegas, NV.

Chung, S.O., and R. Horton. 1987. Soil heat and water-flow with a partial surface mulch. Water Resour. Res. 23:2175–2186.

Constantz, J., S.W. Tyler, and E. Kwicklis. 2003. Temperature-profile methods for estimating percolation rates in arid environments. Vadose Zone J. 2:12–24. doi:10.2136/vzj2003.1200

D'Odorico, P., A. Bhattachan, K.F. Davis, S. Ravi, and C.W. Runyan. 2013. Global desertification: Drivers and feedbacks. Adv. Water Resour. 51:326–344. doi:10.1016/j.advwatres.2012.01.013

Devitt, D.A., L.F. Fenstermaker, M.H. Young, B. Conrad, M. Baghzouz, and B.M. Bird. 2011. Evapotranspiration of mixed shrub communities in phreatophytic zones of the Great Basin region of Nevada (USA). Ecohydrology 4:807–822. doi:10.1002/eco.169

Dixon, J. 1999. An evaluation of unsaturated flow models in an arid climate. M.S. thesis. Univ. of Nevada, Las Vegas. doi:10.2172/759261

Dregne, H., M. Kassas, and B. Rozanov. 1991. A new assessment of the world status of desertification. Desertification Control Bull. 20:6–18.

Durner, W. 1994. Hydraulic conductivity estimation for soil with heterogeneous pore structure. Water Resour. Res. 30:211–223. doi:10.1029/93WR02676

Gee, G.W., J.M. Keller, and A.L. Ward. 2005. Measurement and prediction of deep drainage from bare sediments at a semiarid site. Vadose Zone J. 4:32–40. doi:10.2113/4.1.32

Gee, G.W., P.J. Wierenga, B.J. Andraski, M.H. Young, M.J. Fayer, and M.L. Rockhold. 1994. Variations in water-balance and recharge potential at 3 western desert sites. Soil Sci. Soc. Am. J. 58:63–72. doi:10.2136/sssaj1994.03615995005800010009x

Hare, F.K. 1985. Climate variations, drought and desertification. World Meteorol. Organ., Geneva, Switzerland.

Hill, A.J., T.E. Dawson, O. Shelef, and S. Rachmilevitch. 2015. The role of dew in Negev Desert plants. Oecologia 178:317–327. doi:10.1007/s00442-015-3287-5

Hopmans, J.W., J. Šimůnek, and K.L. Bristow. 2002. Indirect estimation of soil thermal properties and water flux using heat pulse probe measurements: Geometry and dispersion effects. Water Resour. Res. 38(1). doi:10.1029/2000WR000071

Huxman, T.E., K.A. Snyder, D. Tissue, A.J. Leffler, K. Ogle, W.T. Pockman et al. 2004. Precipitation pulses and carbon fluxes in semiarid and arid ecosystems. Oecologia 141:254–268. doi:10.1007/s00442-004-1682-4

Idso, S.B., R.J. Reginato, R.D. Jackson, B.A. Kimball, and F.S. Nakayama. 1974. The three stages of drying of a field soil. Soil Sci. Soc. Am. J. 38:831–837. doi:10.2136/sssaj1974.03615995003800050037x

Kenny, J.F., and K.E. Juracek. 2012. Description of 2005–10 domestic water use for selecting U.S. cities and guidance for estimating domestic water use. USGS, Washington, DC.

Kidron, G.J., and V.P. Gutschick. 2013. Soil moisture correlates with shrub-grass association in the Chihuahuan Desert. Catena 107:71–79. doi:10.1016/j.catena.2013.02.001

Koonce, J.E. 2016. Water balance and moisture dynamics of an arid and semi-arid soil: A weighing lysimeter and field study. Ph.D. diss., Univ. of Nevada, Las Vegas.

Laliberte, G.E., A.T. Corey, and R.H. Brooks. 1966. Properties of unsaturated porous media. Hydrol. Pap. 17. Colorado State Univ., Fort Collins.

Lehmann, P., S. Assouline, and D. Or. 2008. Characteristic lengths affecting evaporative drying of porous media. Phys. Rev. E 77:056309. doi:10.1103/PhysRevE.77.056309

Moreno-de las Heras, M., L. Turnbull, and J. Wainwright. 2016. Seed-bank structure and plant-recruitment conditions regulate the dynamics of a grassland-shrubland Chihuahuan ecotone. Ecology 97:2303–2318. doi:10.1002/ecy.1446

Morgan, J.A., D.E. Pataki, C. Korner, H. Clark, S.J. Del Grosso, J.M. Grunzweig et al. 2004. Water relations in grassland and desert ecosystems exposed to elevated atmospheric CO_2. Oecologia 140:11–25. doi:10.1007/s00442-004-1550-2

Mualem, Y. 1976. A new model for predicting the hydraulic conductivity of unsaturated porous media. Water Resour. Res. 12:513–522. doi:10.1029/WR012i003p00513

Or, D., P. Lehmann, E. Shahraeeni, and N. Shokri. 2013. Advances in soil evaporation physics: A review. Vadose Zone J. 12(4). doi:10.2136/vzj2012.0163

Peters, A., S.C. Iden, and W. Durner. 2015. Revisiting the simplified evaporation method: Identification of hydraulic functions considering vapor, film and corner flow. J. Hydrol. 527:531–542. doi:10.1016/j.jhydrol.2015.05.020

Philip, J.R., and D.A. de Vries. 1957. Moisture movement in porous materials under temperature gradients. Am. Geophys. Union Trans. 38:222–232. doi:10.1029/TR038i002p00222

Priesack, E., and W. Durner. 2006. Closed-form expression for the multimodal unsaturated conductivity function. Vadose Zone J. 5:121–124. doi:10.2136/vzj2005.0066

R Core Team. 2016. R: A language and environment for statistical computing. R Found. Stat. Comput., Vienna.

Rudiyanto, M. Sakai, M.Th. van Genuchten, A.A. Alazba, B.I. Setiawan, and B. Minasny. 2015. A complete soil hydraulic model accounting for capillary and adsorptive water retention, capillary and film conductivity, and hysteresis. Water Resour. Res. 51:8757–8772. doi:10.1002/2015WR017703

Saito, H., J. Šimůnek, and B.P. Mohanty. 2006. Numerical analysis of coupled water, vapor, and heat transport in the vadose zone. Vadose Zone J. 5:784–800. doi:10.2136/vzj2006.0007

Scanlon, B.R., D.G. Levitt, R.C. Reedy, K.E. Keese, and M.J. Sully. 2005. Ecological controls on water-cycle response to climate variability in deserts. Proc. Natl. Acad. Sci. 102:6033–6038.

Shokri, N., P. Lehmann, P. Vontobel, and D. Or. 2008. Drying front and water content dynamics during evaporation from sand delineated by neutron radiography. Water Resour. Res. 44:W06418. doi:10.1029/2007WR006385

Shokri, N., and D. Or. 2011. What determines drying rates at the onset of diffusion controlled stage-2 evaporation from porous media? Water Resour. Res. 47:W09513. doi:10.1029/2010WR010284

Šimůnek, J., M.T. van Genuchten, and M. Sejna. 2016. Recent developments and applications of the HYDRUS computer software packages. Vadose Zone J. 15(7). doi:10.2136/vzj2016.04.0033

Soil Survey Division Staff. 1993. Soil survey manual. Agric. Handb. 18. USDA Soil Conserv. Serv., Washington, DC.

Tuller, M., and D. Or. 2001. Hydraulic conductivity of variably saturated porous media: Film and corner flow in angular pore space. Water Resour. Res. 37:1257–1276. doi:10.1029/2000WR900328

van Genuchten, M.T. 1980. A closed-form equation for predicting the hydraulic conductivity of unsaturated soils. Soil Sci. Soc. Am. J. 44:892–898. doi:10.2136/sssaj1980.03615995004400050002x

Vogel, T., M. Cislerova, and J.W. Hopmans. 1991. Porous media with linearly variable hydraulic properties. Water Resour. Res. 27:2735–2741. doi:10.1029/91WR01676

Western Regional Climate Center. 2017. Cooperative climatological data summaries. Western Regional Clim. Ctr., Reno, NV. http://www.wrcc.dri.edu/cgi-bin/cliMAIN.pl?nv1071 (accessed 7 Apr. 2017